

Transverse and Longitudinal Spin-Torque Ferromagnetic Resonance for Improved Measurement of Spin-Orbit Torque

Saba Karimeddiny^{1,*}, Joseph A. Mittelstaedt^{1,†}, Robert A. Buhrman,¹ and Daniel C. Ralph^{1,2}

¹ Cornell University, Ithaca, New York 14850, USA

² Kavli Institute at Cornell, Ithaca, New York 14853, USA

(Received 18 February 2020; revised 28 June 2020; accepted 16 July 2020; published 11 August 2020)

Spin-torque ferromagnetic resonance (ST-FMR) is a common method used to measure spin-orbit torque (SOT) in heavy-metal/ferromagnet bilayer structures. In the course of a measurement, other resonant processes such as spin pumping (SP) and heating can cause spin-current or heat flows between the layers, inducing additional resonant voltage signals via the inverse spin Hall effect (ISHE) and Nernst effects. In the standard ST-FMR geometry, these extra artifacts exhibit a dependence on the angle of an in-plane magnetic field that is identical to the rectification signal from the SOT. We show experimentally that the rectification and artifact voltages can be quantified separately by measuring the ST-FMR signal transverse to the applied current (i.e., in a Hall geometry) in addition to the usual longitudinal geometry. We find that in Pt(6 nm)/Co₄₀Fe₄₀B₂₀ samples the contribution from the artifacts is small compared with the SOT rectification signal for Co₄₀Fe₄₀B₂₀ layers thinner than 6 nm, but can be significant for thicker magnetic layers. We observe a sign change in the artifact voltage as a function of the Co₄₀Fe₄₀B₂₀ thickness that we suggest may be due to competition between a resonant heating effect and the SP-ISHE contribution.

DOI: 10.1103/PhysRevApplied.14.024024

I. INTRODUCTION

Current-induced spin-orbit torques (SOTs) [1] have the potential to provide improved efficiency in the control of magnetic memory and logic devices, enabling technologies that are fast, nonvolatile, high-density, and of infinite endurance [2–4]. The metrology of SOT materials and devices is critical to these developments. Several different techniques have been developed to quantify spin-orbit torques, including spin-torque ferromagnetic resonance (ST-FMR) [5–8], second-harmonic (low-frequency) Hall measurements [9–11], optical measurements of current-induced magnetic deflection [12,13], determination of the threshold currents for switching of nanoscale magnets with in-plane anisotropy [6,14], measurements of spin Hall magnetoresistance [15,16], and measurements of current-induced domain-wall motion in perpendicular magnetic films [17,18]. However, different techniques sometimes produce inconsistent results [19,20] and can even give internal discrepancies. For example, independent second-harmonic Hall studies on layers with in-plane and out-of-plane magnetic anisotropy [21,22] have measured discrepant (and sometimes unphysical) results for the dampinglike torque efficiency ξ_{DL} , and ST-FMR and

second-harmonic Hall measurements on samples with in-plane anisotropy can differ by tens of percent. Therefore, there is a continuing need to examine possible artifacts affecting the different measurement approaches and to improve their accuracy.

Here we consider one of the most popular techniques for measuring SOTs, ST-FMR. A known artifact in ST-FMR is that the measured signals can include contributions from spin pumping (SP) together with the inverse spin Hall effect (ISHE) [23–26]. In addition, there can be thermoelectric contributions resulting from resonant heating that give rise to a longitudinal spin Seebeck effect (LSSE) together with the ISHE [27,28], or Nernst effects (NEs) [29–32]. In the standard ST-FMR measurement configuration, it is challenging to disentangle these artifact signals from the primary spin-torque diode (rectification) signal, because they all have identical dependences on the angle of a magnetic field applied within the device plane [25,31].

Previous studies attempting to separate artifact voltages from the ST-FMR signal have largely been focused on the SP-ISHE contribution [33–35]. One previous study attempted to separate these contributions by using the external field to tilt the magnetization partly out of the plane [34], but this configuration can be tricky to implement and interpret due to the large demagnetization fields of typical devices and the possibility of spatially nonuniform magnetization states. We demonstrate a straightforward alternative approach to separately quantifying both

*sabakarimeddiny@gmail.com

†These authors contributed equally to this work.

the spin-orbit torque and the spin-pumping and resonant-heating artifact signals using only in-plane magnetic fields, by measuring the ST-FMR signal transverse to the applied current (i.e., in a Hall geometry) in addition to the usual longitudinal geometry.

II. BACKGROUND

In conventional ST-FMR, a microwave current is injected into a rectangular sample of a heavy-metal (HM)/ferromagnet (FM) bilayer to induce FMR through current-induced torques acting on the magnetization. Within a simple macrospin model, the Landau-Lifshitz-Gilbert-Slonczewski (LLGS) equation captures the resulting dynamics of the magnetic moment:

$$\dot{\hat{m}} = \gamma \hat{m} \times \frac{dF}{d\hat{m}} + \alpha \hat{m} \times \dot{\hat{m}} + \tau_{\text{DL}}^0 \hat{m} \times (\hat{\sigma} \times \hat{m}) + \tau_{\text{FL}}^0 \hat{\sigma} \times \hat{m}, \quad (1)$$

where \hat{m} is the normalized magnetic moment of the FM, F is the free-energy density of the FM, $\gamma = 2\mu_B/\hbar$ is the gyromagnetic ratio, with μ_B being the Bohr magneton, and α is the Gilbert damping parameter. The final two terms represent the current-induced dampinglike and fieldlike torques, with prefactors

$$\tau_{\text{DL}}^0 = \xi_{\text{DL}} \frac{\mu_B J_e}{e M_s t_{\text{FM}}}, \quad (2)$$

$$\tau_{\text{FL}}^0 = \xi_{\text{FL}} \frac{\mu_B J_e}{e M_s t_{\text{FM}}}. \quad (3)$$

Here, ξ_{DL} and ξ_{FL} are dimensionless spin-torque efficiencies that one might wish to measure for a given material system. J_e is the charge current density in the HM, e is the magnitude of the electron charge, M_s is the saturation magnetization of the FM, t_{FM} is the thickness of the ferromagnetic layer, and $\hat{\sigma}$ denotes the polarization of the spin current incident on the ferromagnet. For a nonmagnetic heavy metal with an ordinary high-symmetry crystal structure, $\hat{\sigma}$ is required by symmetry to be in-plane and perpendicular to the applied current so that, for an in-plane magnetization, the dampinglike torque points in the sample plane and the fieldlike torque points out of the plane; we assume this to be the case throughout this paper.

The magnetic resonance can be detected via a rectified longitudinal dc voltage (oriented along the length of the wire parallel to the current) caused by mixing of the microwave current with resistance oscillations produced by the precessing magnet via anisotropic magnetoresistance (AMR) or spin Hall magnetoresistance [36,37]. The shape of the resonance peak for this rectified signal as a function of the magnitude of the magnetic field at a constant field angle is a sum of symmetric and antisymmetric

Lorentzian functions. For a magnetic layer with in-plane anisotropy and an in-plane magnetic field, the symmetric component arises from τ_{DL}^0 and the antisymmetric component from a combination of the current-induced Oersted field and τ_{FL}^0 . Once the microwave current is calibrated, the measurement allows determination of both ξ_{DL} and ξ_{FL} , assuming there are no other artifacts contaminating the signal.

When the FM layer is resonantly excited, a pure spin current resulting from SP or the LSSE can also flow from the FM layer into the HM layer and produce a measurable voltage through the ISHE in the HM [23–27,38–41]. Furthermore, an out-of-plane temperature gradient in the heterostructure due to resonant heating can produce a thermoelectric voltage as a result of ordinary or anomalous Nernst effects [28,32]. In all of these processes, the result is a dc voltage perpendicular to the magnetization axis with a symmetric Lorentzian line shape [25,42,43]. Consequently, if these artifact signals are sufficiently large, they can contaminate ST-FMR measurements of τ_{DL}^0 . The signals from spin-torque rectification and from the spin-pumping and resonant-heating artifacts all have the same dependence on the angle of an in-plane magnetic field, proportional to $\sin(2\phi) \cos(\phi)$, with ϕ measured relative to the positive applied-current direction [25,31,33,35], making artifact effects difficult to disentangle.

In this paper, we demonstrate that if one performs a ST-FMR experiment as a function of the angle of an in-plane magnetic field by measuring the resonant dc voltage *transverse* to the current (i.e., in a Hall geometry), the rectified spin-torque contribution and the effects of spin pumping and resonant heating can be distinguished. We are aware of previous studies in which ST-FMR measurements were performed in the transverse geometry [35,44], but these studies did not illustrate how to separate the rectified spin-torque contribution from the artifact signals. A closely related idea had been used previously in experiments that studied SP and ISHE signals from magnetic precession excited using oscillating magnetic fields, in order to separate out unwanted (in that context) rectification signals [38,45]. Harder *et al.* have published a review mapping out the field-angle dependences expected for resonance experiments in both longitudinal and transverse geometries for different orientations of the excitation [46].

III. THEORY

We consider a thin-film macrospin magnet with in-plane anisotropy subject to an external in-plane magnetic field oriented at an angle ϕ with respect to the positive current direction, which aligns the equilibrium direction of the magnetization (see Fig. 1). We define the \hat{y} axis to be parallel to the equilibrium direction of the magnetization and \hat{z} to be perpendicular to the sample plane, so that $\hat{x} = \hat{y} \times \hat{z}$ is in-plane. We use capital letters to indicate a

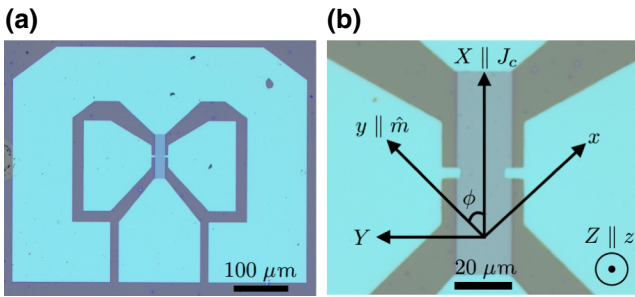


FIG. 1. (a) Optical image of our Hall ST-FMR device, showing the geometry of the contact pads. This particular device features a Pt(6 nm)/Co₄₀Fe₄₀B₂₀(6 nm) bilayer measuring 20 × 80 μm^2 (in the center, dark blue). The scale bar is 100 μm . (b) Enlarged optical image of the bilayer and contacts, with our coordinate definitions. The coordinates X, Y, Z (capitals) are fixed relative to the device geometry, while the coordinates x, y, z (lowercase) are relative to the equilibrium orientation of the magnetization. The scale bar is 20 μm .

separate coordinate system fixed with respect to the sample, where \hat{X} is along the current direction, $\hat{Z} = \hat{z}$, and $\hat{Y} = \hat{Z} \times \hat{X}$. Spherical polar coordinates θ, ϕ for the magnetization orientation are defined relative to the X, Y, Z axes.

A microwave current $I_{\text{rf}} \text{Re}[e^{-i\omega t}]$ is applied, producing alternating torques with amplitudes $\tau_x = \tau_{\text{DL}}^0 \cos(\phi)$ and $\tau_z = \tau_z^0 \cos(\phi) = (\tau_{\text{FL}}^0 + \tau_{\text{OE}}^0) \cos(\phi)$ in the \hat{x} and \hat{z} directions, respectively. With these definitions, τ_{OE}^0 takes a positive value, by Ampère's law, and τ_{DL}^0 is positive for the spin Hall effect in Pt. Linearization and solution of the LLGS equation (see the Supplemental Material [47] and Ref. [8]) allow us to calculate the oscillatory components of the magnetic moment; in complex notation, these are

$$\begin{aligned} m_x &= \frac{-\omega_2 \tau_z + i\omega \tau_x}{-\gamma(B - B_0)\omega^+ + i\alpha\omega\omega^+}, \\ m_z &= \frac{\omega_1 \tau_x + i\omega \tau_z}{-\gamma(B - B_0)\omega^+ + i\alpha\omega\omega^+}. \end{aligned} \quad (4)$$

Here B_0 is the resonance field, B is the applied external field, $\omega_1 = \gamma B_0$, $\omega_2 = \gamma(B_0 + \mu_0 M_{\text{eff}})$, and $\omega^+ = \omega_1 + \omega_2$; M_{eff} is the in-plane saturation magnetization (M_s) minus any out-of-plane anisotropy. Note that, by our definition of the coordinate axes, $m_x = -d\phi$ and $m_z = -d\theta$ during precession.

Assuming that the anisotropic magnetoresistance has the form $R_{XX} = R_0 + R_{\text{AMR}} m_X^2$, the spin-torque mixing voltage in conventional ST-FMR can be written as

$$V_{XX}^{\text{mix}} = \frac{I_{\text{rf}}}{2} R_{\text{AMR}} \text{Re}[m_x] \sin 2\phi, \quad (5)$$

or

$$\begin{aligned} V_{XX}^{\text{mix}} &= \frac{I_{\text{rf}} R_{\text{AMR}}}{2\alpha\omega^+} \sin(2\phi) \cos(\phi) \\ &\times \left(S(B) \tau_{\text{DL}}^0 + A(B) \frac{\omega_2}{\omega} \tau_z^0 \right), \end{aligned} \quad (6)$$

where we define the symmetric Lorentzian $S(B) = \Delta^2 / [(B - B_0)^2 + \Delta^2]$, the antisymmetric Lorentzian $A(B) = (B - B_0)\Delta / [(B - B_0)^2 + \Delta^2]$, and the half-width-at-half-maximum linewidth $\Delta = \alpha\omega/\gamma$. Here R_{AMR} includes contributions from both the anisotropic magnetoresistance in the magnet and the spin Hall magnetoresistance in the Pt layer, as these produce identical contributions to the ST-FMR signal for our sample geometry (see the Supplemental Material [47] and Ref. [48]).

We can compute the transverse spin-torque mixing voltage within the same framework. We assume that the Hall resistance has the symmetry $R_{XY} = R_{\text{PHE}} m_X m_Y + R_{\text{AHE}} m_Z$, where R_{PHE} is the scale of the planar Hall effect (PHE) and R_{AHE} is the scale of the anomalous Hall effect (AHE), in which case [11]

$$V_{XY}^{\text{mix}} = \frac{I_{\text{rf}}}{2} (-R_{\text{PHE}} \cos 2\phi \text{Re}[m_x] + R_{\text{AHE}} \text{Re}[m_z]). \quad (7)$$

Using the results from Eq. (4),

$$\begin{aligned} V_{XY}^{\text{mix}} &= -\frac{I_{\text{rf}} R_{\text{PHE}}}{2\alpha\omega^+} \cos(2\phi) \cos(\phi) \\ &\times \left(S(B) \tau_{\text{DL}}^0 + A(B) \frac{\omega_2}{\omega} \tau_z^0 \right) \\ &+ \frac{I_{\text{rf}} R_{\text{AHE}}}{2\alpha\omega^+} \cos(\phi) \\ &\times \left(S(B) \tau_z^0 - A(B) \frac{\omega_1}{\omega} \tau_{\text{DL}}^0 \right). \end{aligned} \quad (8)$$

The artifact signals due to spin pumping and resonant heating can also contribute to both the longitudinal and the transverse ST-FMR voltage [33–35]. All of the artifacts that we consider, i.e., SP-ISHE contributions, LSSE-ISHE contributions, and NEs, produce resonant dc electric fields that are in-plane and perpendicular to the magnetization axis, and proportional to the square of the precession amplitude (with the precession amplitude proportional to $\cos \phi$). Because these signals depend only on the precession amplitude and not on the phase, they have symmetric line shapes. Taking the components in the longitudinal and transverse directions, the artifact voltages are therefore

$$V_{\text{art}} = E_{\text{art}}^0 S(B) \cos^2 \phi \begin{cases} L \sin \phi & \text{longitudinal,} \\ W \cos \phi & \text{transverse,} \end{cases} \quad (9)$$

where $E_{\text{art}}^0 = E_{\text{SP}}^0 + E_{\text{LSSE}}^0 + E_{\text{NE}}^0$ is the total electric field generated by all artifact signals. The artifact voltages in

the longitudinal and transverse measurements differ only by geometric factors and angular symmetry; L is the device length (parallel to the current flow), and W is the transverse device width.

The electric field due to spin pumping and the inverse spin Hall effect can be calculated by the method of Refs. [23,25,49,50] (see the Supplemental Material [47]):

$$E_{\text{SP}}^0 = \frac{e\theta_{\text{SH}}g_{\text{eff}}^{\uparrow\downarrow}}{2\pi \sum_i \sigma_i t_i} \lambda_{\text{sd}} \tanh\left(\frac{t_{\text{HM}}}{2\lambda_{\text{sd}}}\right) \times \left[\frac{(\tau_{\text{DL}}^0)^2 \omega_1 + (\tau_z^0)^2 \omega_2}{\alpha^2 (\omega^+)^2} \right]. \quad (10)$$

Here θ_{SH} is the spin Hall ratio in the HM (related to the dampinglike spin-torque efficiency by $\theta_{\text{SH}} = \xi_{\text{DL}}/T_{\text{int}}$, where T_{int} is an interfacial spin-transmission factor), $g_{\text{eff}}^{\uparrow\downarrow}$ is the real part of the effective spin-mixing conductance, $\sigma_i(t_i)$ is the charge conductivity (thickness) of layer i , and λ_{sd} is the spin diffusion length of the HM.

If one assumes that the artifacts due to resonant heating by the current-induced torques are proportional to the energy absorbed by the magnetic layer during resonant excitation, the peak dc electric field due to the LSSE and ISHE and to NEs can be calculated similarly [28,30] (see the Supplemental Material [47]):

$$E_{\text{LSSE}}^0 + E_{\text{NE}}^0 = C \frac{M_s t_{\text{FM}} \alpha \omega^+}{2\gamma \sum_i \sigma_i t_i} \left[\frac{(\tau_{\text{DL}}^0)^2 \omega_1 + (\tau_z^0)^2 \omega_2}{\alpha^2 (\omega^+)^2} \right]. \quad (11)$$

Here, C is a material-dependent prefactor. Because of the factor of $t_{\text{FM}} \alpha \omega^+$ in the numerator, the resonant-heating contribution scales differently from the SP-ISHE contribution as a function of the FM thickness, the damping, and the measurement frequency.

Adding the rectification and artifact contributions [and using the fact that $\cos^2 \phi \sin \phi = (\sin 2\phi \cos \phi)/2$ and $\cos^3 \phi = (\cos \phi + \cos 2\phi \cos \phi)/2$], the amplitudes of the symmetric and antisymmetric components of the total longitudinal and transverse ST-FMR signals have the angular dependence

$$\begin{aligned} S_{XX}(\phi) &= S_{XX}^{\text{AMR/art}} \sin 2\phi \cos \phi, \\ A_{XX}(\phi) &= A_{XX}^{\text{AMR}} \sin 2\phi \cos \phi, \\ S_{XY}(\phi) &= S_{XY}^{\text{PHE/art}} \cos 2\phi \cos \phi + S_{XY}^{\text{AHE/art}} \cos \phi, \\ A_{XY}(\phi) &= A_{XY}^{\text{PHE}} \cos 2\phi \cos \phi + A_{XY}^{\text{AHE}} \cos \phi, \end{aligned} \quad (12)$$

with the amplitude coefficients

$$\begin{aligned} S_{XX}^{\text{AMR/art}} &= \frac{I_{\text{rf}}}{2\alpha\omega^+} R_{\text{AMR}} \tau_{\text{DL}}^0 - \frac{L}{2} E_{\text{art}}^0 \\ &\equiv S_{XX}^{\text{AMR}} + V_{\text{art}}, \\ A_{XX}^{\text{AMR}} &= \frac{I_{\text{rf}}}{2\alpha\omega^+} R_{\text{AMR}} \frac{\omega_2}{\omega} \tau_z^0, \\ S_{XY}^{\text{PHE/art}} &= -\frac{I_{\text{rf}}}{2\alpha\omega^+} R_{\text{PHE}} \tau_{\text{DL}}^0 - \frac{W}{2} E_{\text{art}}^0, \\ A_{XY}^{\text{PHE}} &= -\frac{I_{\text{rf}}}{2\alpha\omega^+} R_{\text{PHE}} \frac{\omega_2}{\omega} \tau_z^0, \\ S_{XY}^{\text{AHE/art}} &= \frac{I_{\text{rf}}}{2\alpha\omega^+} R_{\text{AHE}} \tau_z^0 - \frac{W}{2} E_{\text{art}}^0, \\ A_{XY}^{\text{AHE}} &= -\frac{I_{\text{rf}}}{2\alpha\omega^+} R_{\text{AHE}} \frac{\omega_1}{\omega} \tau_{\text{DL}}^0. \end{aligned} \quad (13)$$

One can see that all of the S_{XX} and S_{XY} rectification signals are contaminated by artifact voltages. If one measures just S_{XX} and A_{XX} for in-plane magnetic fields (as in conventional ST-FMR), there is no way to distinguish τ_{DL}^0 from the artifact contributions. However, τ_{DL}^0 appears by itself, without any artifact contamination, in the coefficient A_{XY}^{AHE} . One way to achieve a measurement of τ_{DL}^0 , free of these artifacts, is therefore to directly use the expression for A_{XY}^{AHE} in Eq. (13) along with careful calibration of I_{rf} , α , and R_{AHE} . The out-of-plane torque τ_z^0 can similarly be determined from A_{XX}^{AMR} or A_{XY}^{PHE} . Alternatively, the expressions in Eq. (13) also allow E_{art}^0 and the torque efficiencies ξ_{DL} and ξ_{FL} to be measured without calibrating I_{rf} , α , and the magnetoresistance scales by taking appropriate ratios to cancel prefactors. We can do so using measurements of either the set of parameters $\{S_{XX}^{\text{AMR/art}}, A_{XX}^{\text{AMR}}, S_{XY}^{\text{AHE/art}}, A_{XY}^{\text{AHE}}\}$ or the set $\{S_{XY}^{\text{PHE/art}}, A_{XY}^{\text{PHE}}, S_{XY}^{\text{AHE/art}}, A_{XY}^{\text{AHE}}\}$. We do not expect that the equations involving R_{AMR} and R_{PHE} will be physically independent, because anisotropic magnetoresistance and the planar Hall effect originate from the same microscopic mechanism. Therefore, if the assumptions of our model are correct, these two strategies for taking ratios to cancel prefactors must agree modulo experimental noise. We perform both calculations and test their agreement as a consistency check.

First, using the fact that on resonance $\omega = \sqrt{\omega_1 \omega_2}$, we calculate the ratio $\eta \equiv (\tau_{\text{DL}}^0/\tau_z^0)\sqrt{\omega_1/\omega_2}$, employing the pair of parameters S and A associated with each of the AMR, PHE, and AHE:

$$\eta = \frac{-A_{XY}^{\text{AHE}}}{S_{XY}^{\text{AHE/art}} + W(E_{\text{art}}/2)} = \frac{S_{XY}^{\text{PHE/art}} + W(E_{\text{art}}/2)}{A_{XY}^{\text{PHE}}}, \quad (14a)$$

$$\eta = \frac{S_{XX}^{\text{AMR/art}} + L(E_{\text{art}}/2)}{A_{XX}^{\text{AMR}}}. \quad (14b)$$

Using the measured amplitude coefficients, one can solve separately for E_{art} using either Eq. (14a) or (14b), and check consistency.

It still remains to determine τ_{DL}^0 and to separate the two contributions to $\tau_z^0 = \tau_{\text{FL}}^0 + \tau_{\text{Oe}}^0$. We choose to do this using a method from Ref. [19], in a way that determines both of the spin-torque efficiencies ξ_{DL} and ξ_{FL} at the same time without requiring a separate calibration of I_{rf} . We perform measurements on a series of samples with different thicknesses of the ferromagnetic layer and determine $\eta = (\tau_{\text{DL}}^0 / \tau_z^0) \sqrt{\omega_1 / \omega_2}$ for each sample from any of the expressions in Eqs. (14a) and (14b), after solving for E_{art} . We then define

$$\xi_{\text{FMR}} \equiv \eta \frac{e\mu_0 M_s t_{\text{HM}} t_{\text{FM}}}{\hbar} \sqrt{1 + \frac{\mu_0 M_{\text{eff}}}{B_0}}, \quad (15)$$

so that, using Eqs. (2) and (3) and the fact that $\tau_{\text{Oe}}^0 = \gamma \mu_0 J_e t_{\text{HM}} / 2$ by Ampère's law, we have

$$\frac{1}{\xi_{\text{FMR}}} = \frac{1}{\xi_{\text{DL}}} \left(1 + \frac{\hbar}{e \mu_0 M_s t_{\text{FM}} t_{\text{HM}}} \xi_{\text{FL}} \right). \quad (16)$$

A linear fit of $1/\xi_{\text{FMR}}$ vs $1/t_{\text{FM}}$ can then be used to determine $1/\xi_{\text{DL}}$ (from the intercept) and ξ_{FL} (from the slope).

IV. MEASUREMENTS

We use dc-magnetron sputtering to grow multilayers with the structure substrate/Ta(1 nm)/Pt(6 nm)/ferromagnet (t_{FM})/Al(1 nm), using three different FMs: Co₄₀Fe₄₀B₂₀, permalloy (Ni₈₁Fe₁₉ = Py), and Co₉₀Fe₁₀. Each of the three FMs is expected to have different AMR, PHE, and AHE values, and therefore different strengths of rectified spin-torque signals relative to the artifacts. In particular, Co₄₀Fe₄₀B₂₀ has weak planar magnetoresistances (AMR and PHE), and it has been argued previously that it exhibits a significant contribution from SP and the ISHE in ST-FMR [33,34]. The Co₄₀Fe₄₀B₂₀ devices are grown with $t_{\text{FM}} = \{2, 3, 4, 6, 8, 10\}$ in separate depositions. The Py and Co₉₀Fe₁₀ devices are grown with single relatively large thicknesses to give measurable artifact signals, namely $t_{\text{Py}} = 8$ nm and $t_{\text{Co}_90\text{Fe}_{10}} = 6$ nm. All devices are grown on high-resistivity (greater than $2 \times 10^4 \Omega \text{ cm}$) thermally oxidized silicon wafers to prevent rf current leakage or capacitive coupling. The Ta is used as a seed layer and makes a negligible contribution to the SOTs that we measure, due to the low conductivity of Ta relative to Pt ($\rho_{\text{Pt}} = 20.4 \mu\Omega \text{ cm}$, $\rho_{\text{Co}_40\text{Fe}_{40}\text{B}_{20}} = 110 \mu\Omega \text{ cm}$). The Al cap layer protects the layers below it and is oxidized upon exposure to the atmosphere.

The as-deposited samples are patterned using photolithography and Ar ion-milling to define rectangular bars ranging in size from $20 \mu\text{m} \times 40 \mu\text{m}$ to $40 \mu\text{m} \times 80 \mu\text{m}$

with various aspect ratios. The transverse leads and contact pads are then made using a second photolithography step, in which they are deposited by sputtering a Ti(3 nm)/Pt(75 nm) layer and formed by liftoff so that the side channels extend for a few micrometers on top of the main bar (see Fig. 1). We are careful that the magnetic layer does not extend beyond the defined rectangle into the transverse leads. In early devices, we etch full Hall-bar shapes in the first layer of lithography so that the transverse leads include some of the same magnetic layer as the main channel. For those early devices, we find that the resulting analyses of spin-orbit torque produce anomalous results, varying with the dimensions of the leads and the contact separation. This could possibly be due to spatial nonuniformities in the magnetic orientation and precession, as was speculated in Ref. [44]. Ultimately, the magnetic bilayer is left as simply rectangular to promote uniform precession modes, and this removes the anomalous geometry dependence.

For the ST-FMR measurements, we connect the devices to an amplitude-modulated (AM) microwave source with $f_{\text{AM}} \approx 1700$ Hz through the ac port of a bias tee and to a lock-in amplifier through the dc port; this lock-in amplifier detects the longitudinal signal. Another lock-in amplifier measures the dc voltage across the Hall leads of the device. Both lock-in amplifiers reference the same AM signal, and we collect ST-FMR data in both the longitudinal and the transverse direction simultaneously. An in-plane applied magnetic field is applied at varying angles ϕ using a projected-field magnet. We use fixed microwave frequencies in the range 7–12 GHz and apply 20 dBm of microwave power, and all measurements are performed at room temperature. In Figs. 2(a) and 2(d), we show examples of the detected resonant signals from the parallel (XX) and transverse (XY) lock-in signals for a Pt(6 nm)/Co₄₀Fe₄₀B₂₀(6 nm) sample.

Both the longitudinal and the transverse resonances are fitted well by a sum of symmetric and antisymmetric Lorentzian peaks, with varying relative weights. For each sample, we perform field-swept measurements at a variety of angles ϕ , extracting the symmetric and antisymmetric components of the resonances for both the longitudinal and the transverse signals. The results for a Pt(6 nm)/Co₄₀Fe₄₀B₂₀(6 nm) sample are shown in Figs. 2(b), 2(c), 2(e), and 2(f), along with fits to Eq. (12). Analogous results for Pt(6 nm)/Py(8 nm) and Pt(6 nm)/Co₉₀Fe₁₀(6 nm) samples are shown in the Supplemental Material [47].

We find excellent agreement with the expected angular dependences for S_{XX} , A_{XX} , and A_{XY} . For S_{XY} , the dominant contributions to the angular dependence are, as expected, the $\cos 2\phi \cos \phi$ and $\cos \phi$ terms, but in addition we detect a small component approximately proportional to $\sin 2\phi$. This additional contribution is less than 10% of the larger terms in S_{XY} for all thicknesses of Co₄₀Fe₄₀B₂₀, small enough that it is not included in the fit shown in Fig. 2(e).

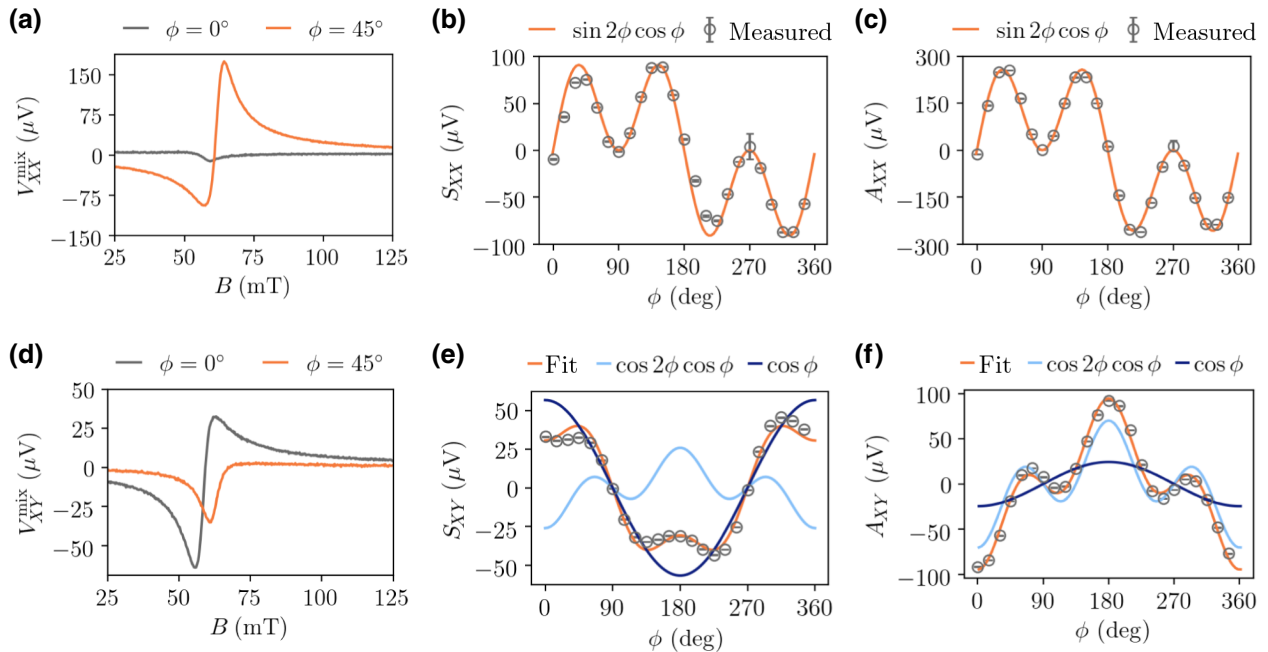


FIG. 2. ST-FMR measurements of a Pt(6 nm)/Co₄₀Fe₄₀B₂₀(6 nm) sample for a measurement frequency $f = 8$ GHz. (a) Longitudinal resonant signals for field sweeps with two different field angles. (b),(c) Symmetric (S_{XX}) and antisymmetric (A_{XX}) Lorentzian fit components for the longitudinal resonant signal as a function of the external-field angle. (d) Transverse resonant signals for field sweeps with two different field angles. (e),(f) Symmetric (S_{XY}) and antisymmetric (A_{XY}) Lorentzian fit components for the transverse resonant signal as a function of the external-field angle. The orange fit line in (b),(c) is a fit to $\sin 2\phi \cos \phi$ (AMR); the light- and dark-blue fit lines in (e),(f) are fits to $\cos 2\phi \cos \phi$ (PHE) and $\cos \phi$ (AHE), respectively, and their sum (orange) fits the data.

It is more significant in the Co₉₀Fe₁₀ and Py samples that we measure, though still smaller than the $\cos 2\phi \cos \phi$ and $\cos \phi$ amplitudes in S_{XY} (see the Supplemental Material [47]). A $\sin 2\phi$ contribution can arise only from a breaking of mirror symmetry relative to the sample's \hat{Y} - \hat{Z} plane (see the Supplemental Material [47]). This symmetry is broken in our samples by the different contact geometries at the two ends of the sample wire [see Fig. 1(a)]. The form of the $\sin 2\phi$ signal can be explained as being due to resonant heating that produces an in-plane thermal gradient in the longitudinal direction of the sample (due, e.g., to differences in heat sinking at the two ends), which is transduced to a transverse voltage with the symmetry of the planar Hall effect (proportional to $m_X m_Y$). We check that the signal is not due to a sample tilt or to a nonresonant dc current that might arise from rectification of the applied microwave signal at the sample contacts. All of the other Fourier components that are the main subject of our analysis maintain the \hat{Y} - \hat{Z} -plane mirror symmetry, and so cannot be altered to first order by a process that breaks this symmetry. Being a separate Fourier component, the $\sin 2\phi$ contribution also does not affect the fits to Eq. (12) used to determine the six amplitude coefficients $S_{XX}^{AMR/art}$, A_{XX}^{AMR} , $S_{XY}^{PHE/art}$, A_{XY}^{PHE} , $S_{XY}^{AHE/art}$, and A_{XY}^{AHE} . Using these coefficients, we calculate E_{art} by solving Eq. (14a) or (14b). There is a potential ambiguity about which roots of Eqs. (14a) and

(14b) to select when applying the quadratic formula. In our measurements, one root would give unphysical results, e.g., a sign change of ξ_{DL} . An important check of our method (and a check that the $\sin 2\phi$ term in S_{XY} does not contaminate the analysis) is that these two independent methods for determining E_{art}^0 [Eqs. (14a) and (14b)] give consistent results. We show below that this is indeed the case.

Figure 3(a) shows the total amplitude of the longitudinal symmetric ST-FMR component (labeled “Measured”), and the corrected value S_{XX}^{AMR} , from which V_{art} has been subtracted. For Co₄₀Fe₄₀B₂₀ layer thicknesses of 6 nm and below, the magnitude of V_{art} is much less than the magnitude of S_{XX}^{AMR} , so that the artifacts have little effect on ST-FMR measurements of the spin-orbit torque. However, with increasing Co₄₀Fe₄₀B₂₀ thickness, the magnitude of S_{XX}^{AMR} decreases and V_{art} grows, and so we find experimentally that for Co₄₀Fe₄₀B₂₀ layers thicker than 6 nm the artifact voltage becomes a significant fraction of the total signal. In this regime, V_{art} and S_{XX}^{AMR} contribute to $S_{XX}(\phi)$ with opposite signs [51], with the consequence that if the artifact contributions are neglected in a conventional ST-FMR analysis, the result is an underestimate of the strength of τ_{DL}^0 . In this respect, our results conflict with some conclusions [33,34] that neglecting the SP-ISHE contribution produces an overestimate of τ_{DL}^0 .

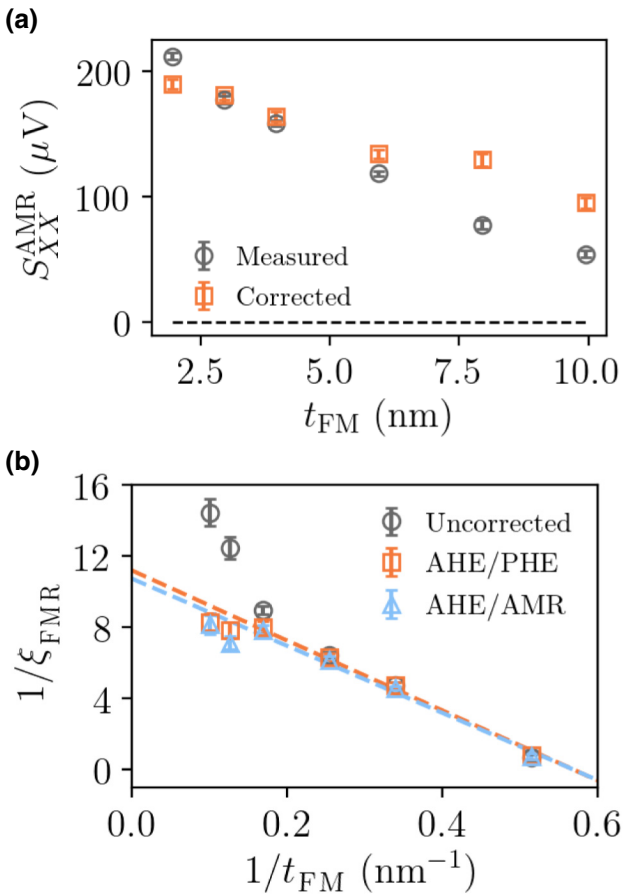


FIG. 3. (a) Uncorrected measured value of S_{XX}^{AMR} vs t_{FM} , together with the value corrected by removing the artifact voltage. (b) Inverse ξ_{FMR} versus inverse t_{FM} . The y intercept of the line is $1/\xi_{\text{DL}}$, and the slope is proportional to ξ_{FL} as in Eq. (16). The two fit lines are color-matched fits to the data points obtained from the AHE-PHE and AHE-AMR corrections.

Analysis of the dependence of $1/\xi_{\text{FMR}}$ as a function of $1/t_{\text{FM}}$ allows a determination of the underlying spin-torque efficiencies ξ_{DL} and ξ_{FL} using Eq. (16). The results for the $\text{Co}_{40}\text{Fe}_{40}\text{B}_{20}$ series of samples are shown in Fig. 3(b). If one does not correct for the contribution of the artifacts, the calculated values of $1/\xi_{\text{FMR}}$ depart upward from the expected linear dependence for $t_{\text{FM}} \gtrsim 6$ nm. Similar results have been reported previously in Ref. [19], where the non-linearity was speculated to arise from SP and the ISHE, and the spin-torque efficiencies were determined by fitting only to results for the thinner FM stacks. After we correct for the artifact contribution, we find good agreement with the expected linear dependence over the full thickness range. From the linear fit, we determine $\xi_{\text{DL}} = 0.090(6)$ and $\xi_{\text{FL}} = -0.020(2)$.

For the Pt(6 nm)/Py(8 nm) and Pt(6 nm)/ $\text{Co}_{90}\text{Fe}_{10}$ (6 nm) samples, we find the same configuration of signs as for the thicker Pt/ $\text{Co}_{40}\text{Fe}_{40}\text{B}_{20}$ samples: V_{art} partially cancels S_{XX}^{AMR} , so that the true mixing signal is larger than the

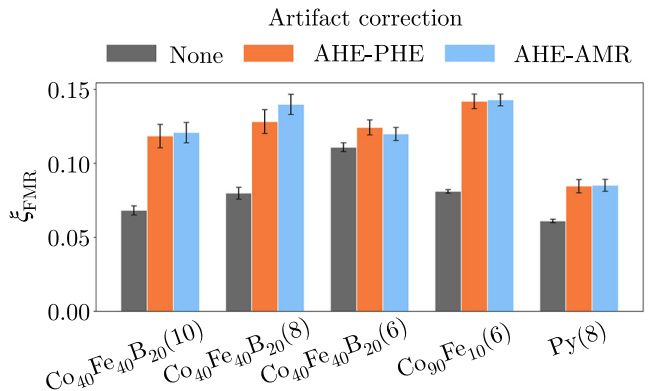


FIG. 4. ξ_{FMR} for various device stacks. The gray (left) bars show values without correction for artifacts, and the orange and blue (center and right) bars show values corrected using the artifact voltages determined from Eqs. (14a) and (14b), respectively.

measured amplitude of $S_{XX}(\phi)$. The results of the calculation of ξ_{FMR} according to Eq. (15) are shown in Fig. 4 for five selected samples, both without and with the correction for artifacts. In determining ξ_{FMR} , we use values for M_s determined by room-temperature vibrating-sample magnetometry (VSM) and values for $\mu_0 M_{\text{eff}}$ determined by fits of the ST-FMR resonant field as a function of frequency. These values are as follows: for $\text{Co}_{40}\text{Fe}_{40}\text{B}_{20}$, $M_s = 9.8 \times 10^5$ A/m and $\mu_0 M_{\text{eff}} = 0.6\text{--}1.4$ T (depending on thickness); for Py, $M_s = 7.5 \times 10^5$ A/m and $\mu_0 M_{\text{eff}} = 1.01$ T; and for $\text{Co}_{90}\text{Fe}_{10}$, $M_s = 9.1 \times 10^5$ A/m and $\mu_0 M_{\text{eff}} = 1.66$ T. If a magnetic dead layer is observed in the VSM measurements, the thickness of the dead layer is subtracted from t_{FM} . In all cases shown in Fig. 4, we find that correcting for the artifact contribution increases our estimates of the values of ξ_{FMR} . The value of ξ_{FMR} is smaller for the Pt/Py sample than for Pt/ $\text{Co}_{40}\text{Fe}_{40}\text{B}_{20}$ or Pt/ $\text{Co}_{90}\text{Fe}_{10}$ primarily because ξ_{FL} both is small and has a positive sign for Pt/Py [52,53].

The dependence of the artifact voltage, V_{art} , on the ferromagnetic-layer thickness is shown in Fig. 5 for the longitudinal ST-FMR component of the Pt/ $\text{Co}_{40}\text{Fe}_{40}\text{B}_{20}$ series of samples. The data are compared with an estimate of the SP-ISHE contribution obtained from Eq. (10), using the following parameters (appropriate for the resistivity of our Pt layers, $\rho_{\text{Pt}} = 20.4 \mu\Omega\text{cm}$): $\theta_{\text{SH}} = 0.32$ [19,54], $g_{\text{eff}}^{\uparrow\downarrow} = 8.26 \times 10^{18} \text{ m}^{-2}$ [54], and $\lambda_{\text{sd}} = 3.7$ nm [55]. The other quantities in Eq. (10) are measured for our samples, including the variation as a function of the $\text{Co}_{40}\text{Fe}_{40}\text{B}_{20}$ thickness. The comparison therefore includes no adjustable fitting parameters, but given that there is considerable disagreement in the literature about the values of the parameters θ_{SH} , $g_{\text{eff}}^{\uparrow\downarrow}$, and λ_{sd} , one should still be careful about drawing quantitative conclusions. The comparison indicates to us that for the samples with $t_{\text{FM}} \geq 3$ nm, the

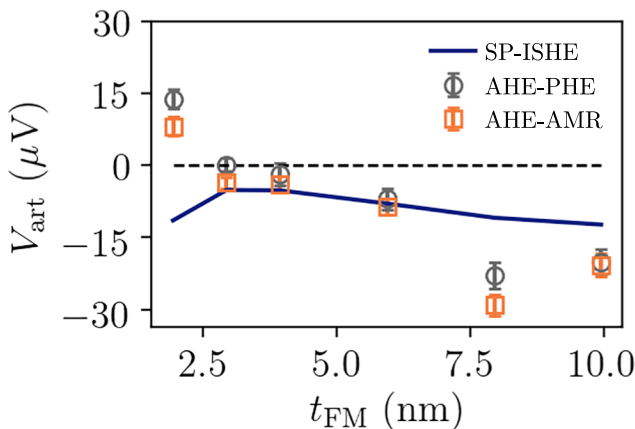


FIG. 5. Artifact voltage as a function of the FM thickness in Pt(6 nm)/Co₄₀Fe₄₀B₂₀ samples. The two types of data point reflect the two correction equations [Eqs. (14a) and (14b)]. The line is the estimated SP-ISHE contribution, determined using the parameters described in the text, with no adjustable parameters.

SP-ISHE theory predicts the correct sign and can roughly capture the overall magnitude and thickness dependence of the measured artifact signal. However, the measured artifact voltage for $t_{\text{FM}} = 2$ nm has the opposite sign, inconsistent with SP and the ISHE. We are confident that the measured sign change is real, because we measure and perform the analysis on five Pt(6 nm)/Co₄₀Fe₄₀B₂₀(2 nm) devices with varied geometries, with consistent results.

Given that SP and the ISHE cannot explain the sign change in the artifact voltage for our $t_{\text{FM}} = 2$ nm samples, we suggest that resonant heating effects might be comparable to the effects of SP and the ISHE in our Pt(6 nm)/Co₄₀Fe₄₀B₂₀ samples, with sufficient strength to reverse the overall sign of the artifact voltage for our thinnest samples. This suggestion differs from one made in previous studies on Pt/ytrrium iron garnet (YIG) samples, in which frequency-dependent measurements demonstrated that SP and ISHE signals dominate over resonant-heating artifacts [43,56]. However, the relative strength of the heating effects and of SP and SHE should scale in proportion to the damping α [compare Eqs. (10) and (11)], so that the heating effects should be more significant in higher-damping ferromagnetic metals than in the lower-damping YIG. We calculate that the resonant heating due to excitation of magnetic precession in our 2-nm samples is approximately $2.5 \times 10^4 \text{ W m}^{-2}$ (see the Supplemental Material [47]), only about a factor of 5 less than the ohmic heating per unit area in the Co₄₀Fe₄₀B₂₀, approximately $1.2 \times 10^5 \text{ W m}^{-2}$. We suggest that this is sufficient to measurably alter the thermal gradients within the sample at resonance and induce resonant signals arising from the LSSE and/or from Nernst effects. Because of an increase in the damping coefficient α with decreasing magnetic thickness, the ratio of resonant heating to ohmic heating

is significantly greater for the 2-nm Co₄₀Fe₄₀B₂₀ samples than for the thicker magnetic layers (see the Supplemental Material [47]).

As noted in the Introduction, past experiments have shown a discrepancy between measurements of ξ_{DL} using low-frequency second-harmonic Hall and ST-FMR techniques. To see if our correction for the artifact voltages in ST-FMR alleviates the discrepancy between the two techniques, we carry out low-frequency second-harmonic Hall measurements on the same Pt/Co₄₀Fe₄₀B₂₀ bilayers (see Appendix). We find that the low-frequency second-harmonic measurements of ξ_{DL} are still approximately 60% larger than what we measure by ST-FMR, even after correcting the ST-FMR measurements for spin pumping and resonant heating. This persisting quantitative difference suggests that the assumptions used in analyzing one or both of these experiments are missing an important piece of physics. Our analysis indicates that this missing physics is not simply the neglect of spin pumping or the effect of a simple heating-induced voltage in the ST-FMR results, and therefore more work must be done to understand the source of the disagreement.

V. CONCLUSION

In conclusion, we demonstrate that the rectification signal used to measure the strength of the spin-orbit torque in ST-FMR can be separated from artifact voltages that may arise due to spin pumping and resonant heating by performing ST-FMR in the transverse (Hall) configuration as well as in the usual longitudinal configuration. For Pt(6 nm)/Co₄₀Fe₄₀B₂₀(t_{FM}) samples, the artifact voltages are small compared with the rectification signal for $t_{\text{FM}} < 6$ nm, but they can become a significant part of the measured signal for thicker magnetic layers. The sign and overall magnitude of the measured artifact voltage for these thicker layers are consistent with expectations for the SP-ISHE signal. However, the sign of the artifact voltage is reversed for our thinnest magnetic layers, with $t_{\text{FM}} = 2$ nm. This sign reversal cannot be explained by SP and the ISHE, and so we suggest that it may be caused by a resonant heating effect.

ACKNOWLEDGMENTS

This research was supported in part by Task 2776.047 of ASCENT, one of six centers in JUMP, a Semiconductor Research Corporation program sponsored by DARPA, and in part by the National Science Foundation (Grant No. DMR-1708499). The devices were fabricated using the shared facilities of the Cornell NanoScale Facility, a member of the National Nanotechnology Coordinated Infrastructure (NNCI), and the Cornell Center for Materials Research, both of which are supported by the NSF (Grants No. NNCI-1542081 and No. DMR-1719875).

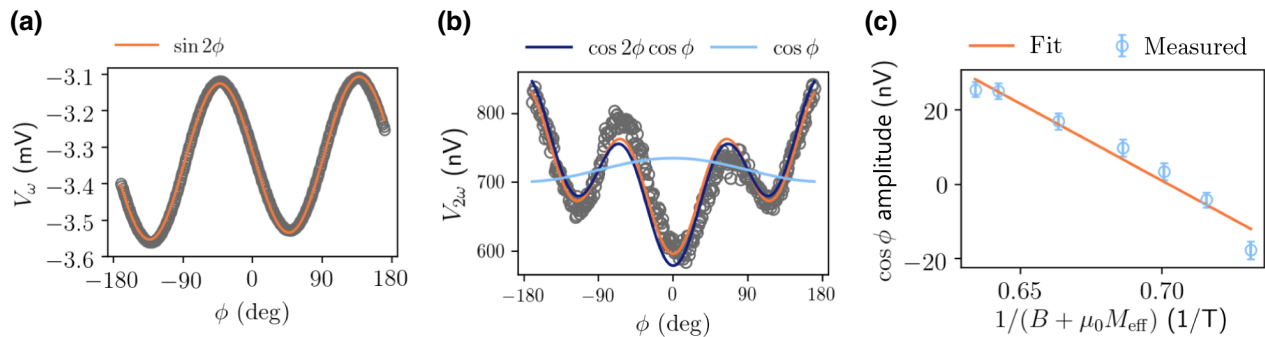


FIG. 6. (a) Angular dependence of the first-harmonic Hall voltage, which allows extraction of the planar Hall resistance. (b) Angular dependence of the second-harmonic Hall voltage, showing the decomposition into $\cos \phi$ (light blue) and $\cos 2\phi \cos \phi$ (dark blue) components, which are related to the dampinglike and fieldlike torques, respectively. (c) Field dependence of the amplitude of the $\cos \phi$ component of the second-harmonic Hall voltage. The slope of this line is related to the dampinglike torque and the intercept to the anomalous Nernst voltage. All data shown here are from measurements on a sample with 8 nm of $\text{Co}_{40}\text{Fe}_{40}\text{B}_{20}$.

APPENDIX: LOW-FREQUENCY SECOND-HARMONIC HALL MEASUREMENTS

It is widely known (but not explained clearly in the literature) that resonant ST-FMR measurements and non-resonant second-harmonic Hall measurements of spin-orbit torque can differ even for identical layer structures, with results from the low-frequency second-harmonic Hall measurements resulting in spin Hall torque efficiencies that are larger by tens of percent. Since our correction to the ST-FMR for the presence of artifact voltages tends to increase the measured spin Hall torque efficiency, we perform second-harmonic Hall measurements on our samples to see if the discrepancy seen in previous measurements can be explained.

We carry out these measurements on standard Hall-bar-shaped devices patterned on the same samples that we use for our ST-FMR devices. We perform these measurements on samples with 2- and 8-nm-thick $\text{Co}_{40}\text{Fe}_{40}\text{B}_{20}$ layers, since these samples represent the extremes of the effect of the artifact voltage on ST-FMR measurements. We employ the standard methodology for investigating in-plane-magnetized samples [31], which involves measuring the first- and second-harmonic Hall response as a function of the in-plane external-field angle. The fitting functions that we use for the first and second harmonics are

$$V_\omega = \frac{IR_{\text{PHE}}}{2} \sin 2\phi, \quad (\text{A1})$$

$$V_{2\omega} = IR_{\text{PHE}} \frac{\tau_z^0}{\gamma} \frac{\cos 2\phi \cos \phi}{B} - \left(\frac{IR_{\text{AHE}}}{2} \frac{\tau_x^0}{\gamma} \frac{1}{B + \mu_0 M_{\text{eff}}} + V_{\text{ANE}} \right) \cos \phi, \quad (\text{A2})$$

where I is the current in the bar, and V_{ANE} is the thermal voltage due to the anomalous Nernst effect. The angle-dependent data and fits are shown in Figs. 6(a) and 6(b) for

an 8-nm thick $\text{Co}_{40}\text{Fe}_{40}\text{B}_{20}$ sample with a 2000-G applied external field.

The dampinglike torque can be obtained from the magnetic field dependence of the amplitude of the $\cos \phi$ part of the second-harmonic voltage [Fig. 6(c)]. The amplitude of the $\cos \phi$ contribution follows the expected linear trend well. From this, we obtain a dampinglike torque efficiency of $\xi_{\text{DL}} = 0.147 \pm 0.003$ for the 2-nm $\text{Co}_{40}\text{Fe}_{40}\text{B}_{20}$ film and 0.145 ± 0.008 for the 8-nm film, both roughly 60% higher than for the corrected ST-FMR measurements. The discrepancy in the dampinglike torque efficiency between the two measurement techniques remains, indicating that the artifact voltages that we correct for in this paper cannot explain the difference.

- [1] J. Slonczewski, Current-driven excitation of magnetic multilayers, *J. Magn. Magn. Mater.* **159**, L1 (1996).
- [2] A. Brataas, A. D. Kent, and H. Ohno, Current-induced torques in magnetic materials, *Nat. Mater.* **11**, 372 (2012).
- [3] K. L. Wang, J. G. Alzate, and P. K. Amiri, Low-power non-volatile spintronic memory: STT-RAM and beyond, *J. Phys. D: Appl. Phys.* **46**, 074003 (2013).
- [4] F. Oboril, R. Bishnoi, M. Ebrahimi, and M. B. Tahoori, Evaluation of hybrid memory technologies using SOT-MRAM for on-chip cache hierarchy, *IEEE Trans. Comput.-Aided Des. Integrated Circuits Syst.* **34**, 367 (2015).
- [5] L. Liu, T. Moriyama, D. C. Ralph, and R. A. Buhrman, Spin-Torque Ferromagnetic Resonance Induced by the Spin Hall Effect, *Phys. Rev. Lett.* **106**, 036601 (2011).
- [6] L. Liu, C.-F. Pai, Y. Li, H. W. Tseng, D. C. Ralph, and R. A. Buhrman, Spin-torque switching with the giant spin Hall effect of tantalum, *Science* **336**, 555 (2012).
- [7] A. R. Mellnik, J. S. Lee, A. Richardella, J. L. Grab, P. J. Mintun, M. H. Fischer, A. Vaezi, A. Manchon, E.-A. Kim, N. Samarth, and D. C. Ralph, Spin-transfer torque generated by a topological insulator, *Nature* **511**, 449 (2014).

- [8] M. Harder, Z. X. Cao, Y. S. Gui, X. L. Fan, and C.-M. Hu, Analysis of the line shape of electrically detected ferromagnetic resonance, *Phys. Rev. B* **84**, 054423 (2011).
- [9] U. H. Pi, K. Won Kim, J. Y. Bae, S. C. Lee, Y. J. Cho, K. S. Kim, and S. Seo, Tilting of the spin orientation induced by Rashba effect in ferromagnetic metal layer, *Appl. Phys. Lett.* **97**, 162507 (2010).
- [10] K. Garello, I. M. Miron, C. O. Avci, F. Freimuth, Y. Mokrousov, S. Blügel, S. Auffret, O. Boulle, G. Gaudin, and P. Gambardella, Symmetry and magnitude of spin-orbit torques in ferromagnetic heterostructures, *Nat. Nanotechnol.* **8**, 587 (2013).
- [11] M. Hayashi, J. Kim, M. Yamanouchi, and H. Ohno, Quantitative characterization of the spin-orbit torque using harmonic Hall voltage measurements, *Phys. Rev. B* **89**, 144425 (2014).
- [12] X. Fan, H. Celik, J. Wu, C. Ni, K.-J. Lee, V. O. Lorenz, and J. Q. Xiao, Quantifying interface and bulk contributions to spin-orbit torque in magnetic bilayers, *Nat. Commun.* **5**, 3042 (2014).
- [13] X. Fan, A. R. Mellnik, W. Wang, N. Reynolds, T. Wang, H. Celik, V. O. Lorenz, D. C. Ralph, and J. Q. Xiao, All-optical vector measurement of spin-orbit-induced torques using both polar and quadratic magneto-optic Kerr effects, *Appl. Phys. Lett.* **109**, 122406 (2016).
- [14] J. Z. Sun, Spin-current interaction with a monodomain magnetic body: A model study, *Phys. Rev. B* **62**, 570 (2000).
- [15] M. Althammer *et al.*, Quantitative study of the spin Hall magnetoresistance in ferromagnetic insulator/normal metal hybrids, *Phys. Rev. B* **87**, 224401 (2013).
- [16] J. Kim, P. Sheng, S. Takahashi, S. Mitani, and M. Hayashi, Spin Hall Magnetoresistance in Metallic Bilayers, *Phys. Rev. Lett.* **116**, 097201 (2016).
- [17] S. Emori, E. Martinez, K.-J. Lee, H.-W. Lee, U. Bauer, S.-M. Ahn, P. Agrawal, D. C. Bono, and G. S. D. Beach, Spin Hall torque magnetometry of Dzyaloshinskii domain walls, *Phys. Rev. B* **90**, 184427 (2014).
- [18] C.-F. Pai, M. Mann, A. J. Tan, and G. S. D. Beach, Determination of spin torque efficiencies in heterostructures with perpendicular magnetic anisotropy, *Phys. Rev. B* **93**, 144409 (2016).
- [19] C.-F. Pai, Y. Ou, L. H. Vilela-Leão, D. C. Ralph, and R. A. Buhrman, Dependence of the efficiency of spin Hall torque on the transparency of Pt/ferromagnetic layer interfaces, *Phys. Rev. B* **92**, 064426 (2015).
- [20] X. Tao, Q. Liu, B. Miao, R. Yu, Z. Feng, L. Sun, B. You, J. Du, K. Chen, S. Zhang, L. Zhang, Z. Yuan, D. Wu, and H. Ding, Self-consistent determination of spin Hall angle and spin diffusion length in Pt and Pd: The role of the interface spin loss, *Sci. Adv.* **4**, 1670 (2018).
- [21] L. Zhu, K. Sobotkiewich, X. Ma, X. Li, D. C. Ralph, and R. A. Buhrman, Strong damping-like spin-orbit torque and tunable Dzyaloshinskii–Moriya interaction generated by low-resistivity $Pd_{1-x}Pt_x$ alloys, *Adv. Funct. Mater.* **29**, 1805822 (2019).
- [22] Y.-C. Lau and M. Hayashi, Spin torque efficiency of Ta, W, and Pt in metallic bilayers evaluated by harmonic Hall and spin Hall magnetoresistance measurements, *Jpn. J. Appl. Phys.* **56**, 0802B5 (2017).
- [23] Y. Tserkovnyak, A. Brataas, and G. E. W. Bauer, Enhanced Gilbert Damping in Thin Ferromagnetic Films, *Phys. Rev. Lett.* **88**, 117601 (2002).
- [24] Y. Tserkovnyak, A. Brataas, and G. E. W. Bauer, Spin pumping and magnetization dynamics in metallic multilayers, *Phys. Rev. B* **66**, 224403 (2002).
- [25] O. Mosendz, V. Vlaminck, J. E. Pearson, F. Y. Fradin, G. E. W. Bauer, S. D. Bader, and A. Hoffmann, Detection and quantification of inverse spin Hall effect from spin pumping in permalloy/normal metal bilayers, *Phys. Rev. B* **82**, 214403 (2010).
- [26] A. Azevedo, L. H. Vilela-Leão, R. L. Rodríguez-Suárez, A. F. Lacerda Santos, and S. M. Rezende, Spin pumping and anisotropic magnetoresistance voltages in magnetic bilayers: Theory and experiment, *Phys. Rev. B* **83**, 144402 (2011).
- [27] K.-i. Uchida, H. Adachi, T. Ota, H. Nakayama, S. Maekawa, and E. Saitoh, Observation of longitudinal spin-Seebeck effect in magnetic insulators, *Appl. Phys. Lett.* **97**, 172505 (2010).
- [28] J. Holanda, O. Alves Santos, R. L. Rodríguez-Suárez, A. Azevedo, and S. M. Rezende, Simultaneous spin pumping and spin Seebeck experiments with thermal control of the magnetic damping in bilayers of yttrium iron garnet and heavy metals: YIG/Pt and YIG/IrMn, *Phys. Rev. B* **95**, 134432 (2017).
- [29] K.-D. Lee, D.-J. Kim, H. Yeon Lee, S.-H. Kim, J.-H. Lee, K.-M. Lee, J.-R. Jeong, K.-S. Lee, H.-S. Song, J.-W. Sohn, S.-C. Shin, and B.-G. Park, Thermoelectric signal enhancement by reconciling the spin Seebeck and anomalous Nernst effects in ferromagnet/non-magnet multilayers, *Sci. Rep.* **5**, 10249 (2015).
- [30] T. Kikkawa, K. Uchida, Y. Shiomi, Z. Qiu, D. Hou, D. Tian, H. Nakayama, X.-F. Jin, and E. Saitoh, Longitudinal Spin Seebeck Effect Free from the Proximity Nernst Effect, *Phys. Rev. Lett.* **110**, 067207 (2013).
- [31] C. O. Avci, K. Garello, M. Gabureac, A. Ghosh, A. Fuhrer, S. F. Alvarado, and P. Gambardella, Interplay of spin-orbit torque and thermoelectric effects in ferromagnet/normal-metal bilayers, *Phys. Rev. B* **90**, 224427 (2014).
- [32] N. Roschewsky, E. S. Walker, P. Gowtham, S. Muschinske, F. Hellman, S. R. Bank, and S. Salahuddin, Spin-orbit torque and Nernst effect in Bi-Sb/Co heterostructures, *Phys. Rev. B* **99**, 195103 (2019).
- [33] K. Kondou, H. Sukegawa, S. Kasai, S. Mitani, Y. Niimi, and Y. Otani, Influence of inverse spin Hall effect in spin-torque ferromagnetic resonance measurements, *Appl. Phys. Express* **9**, 023002 (2016).
- [34] A. Okada, Y. Takeuchi, K. Furuya, C. Zhang, H. Sato, S. Fukami, and H. Ohno, Spin-Pumping-Free Determination of Spin-Orbit Torque Efficiency from Spin-Torque Ferromagnetic Resonance, *Phys. Rev. Appl.* **12**, 014040 (2019).
- [35] A. Kumar, S. Akansel, H. Stopfel, M. Fazlali, J. Åkerman, R. Brucas, and P. Svedlindh, Spin transfer torque ferromagnetic resonance induced spin pumping in the Fe/Pd bilayer system, *Phys. Rev. B* **95**, 064406 (2017).
- [36] A. Tulapurkar, Y. Suzuki, A. Fukushima, H. Kubota, H. Maehara, K. Tsunekawa, D. Djayaprawira, N. Watanabe, and S. Yuasa, Spin-torque diode effect in magnetic tunnel junctions, *Nature* **438**, 339 (2005).

- [37] J. C. Sankey, P. M. Braganca, A. G. F. Garcia, I. N. Krivorotov, R. A. Buhrman, and D. C. Ralph, Spin-Transfer-Driven Ferromagnetic Resonance of Individual Nanomagnets, *Phys. Rev. Lett.* **96**, 227601 (2006).
- [38] J. Lustikova, Y. Shiomi, and E. Saitoh, Vector spectroscopy for spin pumping, *Phys. Rev. B* **92**, 224436 (2015).
- [39] M. B. Jungfleisch, A. V. Chumak, A. Kehlberger, V. Lauer, D. H. Kim, M. C. Onbasli, C. A. Ross, M. Kläui, and B. Hillebrands, Thickness and power dependence of the spin-pumping effect in $\text{Y}_3\text{Fe}_5\text{O}_{12}/\text{Pt}$ heterostructures measured by the inverse spin Hall effect, *Phys. Rev. B* **91**, 134407 (2015).
- [40] H. Nakayama, K. Ando, K. Harii, T. Yoshino, R. Takahashi, Y. Kajiwara, K. Uchida, Y. Fujikawa, and E. Saitoh, Geometry dependence on inverse spin Hall effect induced by spin pumping in $\text{Ni}_{81}\text{Fe}_{19}/\text{Pt}$ films, *Phys. Rev. B* **85**, 144408 (2012).
- [41] S. M. Rezende, R. L. Rodríguez-Suárez, R. O. Cunha, A. R. Rodrigues, F. L. A. Machado, G. A. Fonseca Guerra, J. C. Lopez Ortiz, and A. Azevedo, Magnon spin-current theory for the longitudinal spin-Seebeck effect, *Phys. Rev. B* **89**, 014416 (2014).
- [42] E. Saitoh, M. Ueda, H. Miyajima, and G. Tatara, Conversion of spin current into charge current at room temperature: Inverse spin-Hall effect, *Appl. Phys. Lett.* **88**, 182509 (2006).
- [43] R. Iguchi and E. Saitoh, Measurement of spin pumping voltage separated from extrinsic microwave effects, *J. Phys. Soc. Jpn.* **86**, 011003 (2017).
- [44] A. Bose, S. Dutta, S. Bhuktare, H. Singh, and A. A. Tulaipurkar, Sensitive measurement of spin-orbit torque driven ferromagnetic resonance detected by planar Hall geometry, *Appl. Phys. Lett.* **111**, 162405 (2017).
- [45] S. Keller, J. Greser, M. R. Schweizer, A. Conca, V. Lauer, C. Dubs, B. Hillebrands, and E. T. Papaioannou, Relative weight of the inverse spin-Hall and spin-rectification effects for metallic polycrystalline Py/Pt, epitaxial Fe/Pt, and insulating YIG/Pt bilayers: Angular dependent spin pumping measurements, *Phys. Rev. B* **96**, 024437 (2017).
- [46] M. Harder, Y. Gui, and C.-M. Hu, Electrical detection of magnetization dynamics via spin rectification effects, *Phys. Rep.* **661**, 1 (2016), electrical detection of magnetization dynamics via spin rectification effects.
- [47] See Supplemental Material at <http://link.aps.org/supplemental/10.1103/PhysRevApplied.14.024024> for derivations of the signals expected from ST-FMR, spin pumping, and thermal effects. Additionally, we show the dependence of the artifacts on the microwave power, VSM data on the $\text{Co}_{40}\text{Fe}_{40}\text{B}_{20}$ material, and ST-FMR data for Py and $\text{Co}_{90}\text{Fe}_{10}$.
- [48] N. Vlietstra, J. Shan, V. Castel, B. J. van Wees, and J. Ben Youssef, Spin-Hall magnetoresistance in platinum on yttrium iron garnet: Dependence on platinum thickness and in-plane/out-of-plane magnetization, *Phys. Rev. B* **87**, 184421 (2013).
- [49] S. Mizukami, Y. Ando, and T. Miyazaki, The study on ferromagnetic resonance linewidth for NM/80NiFe/NM (NM = Cu, Ta, Pd and Pt) films, *Jpn. J. Appl. Phys.* **40**, 580 (2001).
- [50] A. Brataas, Y. Tserkovnyak, G. E. W. Bauer, and P. J. Kelly, Spin pumping and spin transfer, arXiv:1108.0385 (2011).
- [51] M. Schreier, G. E. W. Bauer, V. I. Vasyuchka, J. Flipse, K. ichi Uchida, J. Lotze, V. Lauer, A. V. Chumak, A. A. Serga, S. Daimon, T. Kikkawa, E. Saitoh, B. J. van Wees, B. Hillebrands, R. Gross, and S. T. B. Goennenwein, Sign of inverse spin Hall voltages generated by ferromagnetic resonance and temperature gradients in yttrium iron garnet platinum bilayers, *J. Phys. D: Appl. Phys.* **48**, 025001 (2014).
- [52] X. Fan, J. Wu, Y. Chen, M. J. Jerry, H. Zhang, and J. Q. Xiao, Observation of the nonlocal spin-orbital effective field, *Nat. Commun.* **4**, 1799 (2013).
- [53] T. Nan, S. Emori, C. T. Boone, X. Wang, T. M. Oxholm, J. G. Jones, B. M. Howe, G. J. Brown, and N. X. Sun, Comparison of spin-orbit torques and spin pumping across NiFe/Pt and NiFe/Cu/Pt interfaces, *Phys. Rev. B* **91**, 214416 (2015).
- [54] L. Zhu, D. C. Ralph, and R. A. Buhrman, Effective Spin-Mixing Conductance of Heavy-Metal–Ferromagnet Interfaces, *Phys. Rev. Lett.* **123**, 057203 (2019).
- [55] M.-H. Nguyen, D. C. Ralph, and R. A. Buhrman, Spin Torque Study of the Spin Hall Conductivity and Spin Diffusion Length in Platinum Thin Films with Varying Resistivity, *Phys. Rev. Lett.* **116**, 126601 (2016).
- [56] R. Iguchi, K. Ando, R. Takahashi, T. An, E. Saitoh, and T. Sato, Spin pumping without three-magnon splitting in polycrystalline $\text{Bi}_1\text{Y}_2\text{Fe}_5\text{O}_{12}/\text{Pt}$ bilayer structure, *Jpn. J. Appl. Phys.* **51**, 103004 (2012).